Chinese Chemical Letters 35 (2024) 109113

Contents lists available at ScienceDirect

Chinese Chemical Letters

journal homepage: www.elsevier.com/locate/cclet

Supramolecular phenolic network-engineered C–CeO_2 nanofibers for simultaneous determination of isoniazid and hydrazine in biological fluids

Gang Lang[a], Jing Feng[a,b,*], Bo Feng[c], Junlan Hu[a], Zhiling Ran[a], Zhiting Zhou[a], Zhenju Jiang[a], Yunxiang He[b], Junling Guo[b,d,e,f,*]

[a] School of Science, Xihua University, Chengdu 610039, China
[b] BMI Center for Biomass Materials and Nanointerfaces, College of Biomass Science and Engineering, Sichuan University, Chengdu 610065, China
[c] Southwest Computer Co., Ltd., Chongqing 400060, China
[d] Bioproducts Institute, Department of Chemical and Biological Engineering, The University of British Columbia, Vancouver V6T 1Z4, Canada
[e] State Key Laboratory of Polymer Materials Engineering, Sichuan University, Chengdu 610065, China
[f] National Engineering Laboratory for Clean Technology of Leather Manufacture Sichuan University, Chengdu 610065, China

ARTICLE INFO

Article history:
Received 28 April 2023
Revised 23 August 2023
Accepted 15 September 2023
Available online 17 September 2023

Keywords:
Electrochemical detection
Therapeutic drug monitoring
Isoniazid
Hydrazine
Tuberculosis

ABSTRACT

Electrochemical sensing provides a powerful technological means for the therapeutic drug monitoring of drug-resistant tuberculosis but requires a functionalized electrode to capture the analytes and catalyze their redox reactions. Herein, we construct a nickel–tannic acid supramolecular network (Ni–TA) on the surface of electrospun-derived C–CeO_2 nanofiber for the sensitive and simultaneous detection of isoniazid (INZ) and hydrazine (HYD). Mechanistic investigations demonstrate that Ni–TA is electronegative and hydrophilic, thus facilitating an efficient mass and electron transfer. Ni–TA/C–CeO_2 has higher adsorption rate constants (0.091 g mg^{-1} h^{-1} for INZ, and 0.062 g mg^{-1} h^{-1} for HYD) than native C–CeO_2 (0.075 g mg^{-1} h^{-1} for INZ, and 0.047 g mg^{-1} h^{-1} for HYD). Moreover, Ni–TA/C–CeO_2 (56 Ω) has lower charge transfer resistances than C–CeO_2 (417 Ω). Ni–TA/C–CeO_2 performs low detection limits and wide linearity ranges for INZ (0.012 μmol/L and 0.1–400 μmol/L, respectively) and HYD (0.008 μmol/L and 0.015–1420 μmol/L, respectively), coupled with high selectivity, cycle stability and reproducibility. This research demonstrated the promising applications of Ni–TA/C–CeO_2 by analyzing human-collected plasma and urine samples.

Drug-resistant tuberculosis is a global leading cause of death by an infectious disease and poses a serious therapeutic challenge. Isoniazid (INZ) is a widely used antibiotic for tuberculosis treatment [1], while hydrazine (HYD), a carcinogenic, hepatotoxic, neurotoxic substance, is a byproduct of INZ metabolism that can also severely impact the respiratory system [2,3]. Thus, rapid and straightforward monitoring of INZ and HYD metabolic changes is critical in ensuring the efficacy of this medication in combating tuberculosis, by providing timely data on drug concentrations in body fluids (*e.g.*, blood and urine) to better guide therapy and minimize side effects [4]. Therefore, the development of an easy-to-use and efficient analytical tool for the precise and simultaneous detection of INZ and HYD is crucial for clinical diagnosis and nursing.

Electrochemical sensing with unique features in respect of low cost, fast response, easy operation, and feasible miniaturization, is an ideal platform for the detection of INZ and HYD [5,6]. However, it requires a functionalized electrode to capture the analytes, catalyze the redox reaction of analytes, and thus realize sensitive detection [7]. The main challenge in improving the detection sensitivity is to facilitate the mass transport on the surface of the electrode, as mass transport is usually the rate-controlling step of inhomogeneous reaction [8]. C–CeO_2 nanofiber is a prominent electrocatalyst for its excellent adsorption properties and tunable physical/chemical properties of the surface [9,10]. The coexistence of Ce^{III} and Ce^{IV} on its surface endows it with abundant active sites for the adsorbed species which would facilitate the mass transport on the surface of the electrode. In addition, according to the space charge theory, constructing a metal coordination interface could largely improve the mass transport of reactants [11]. Metal-phenolic networks (MPNs) is a versatile class of self-assembled supramolecular materials constructed from phe-

* Corresponding authors.
E-mail addresses: jingfeng@mail.xhu.edu.cn (J. Feng), junling.guo@scu.edu.cn, junling.guo@ubc.ca (J. Guo).

https://doi.org/10.1016/j.cclet.2023.109113
1001-8417/

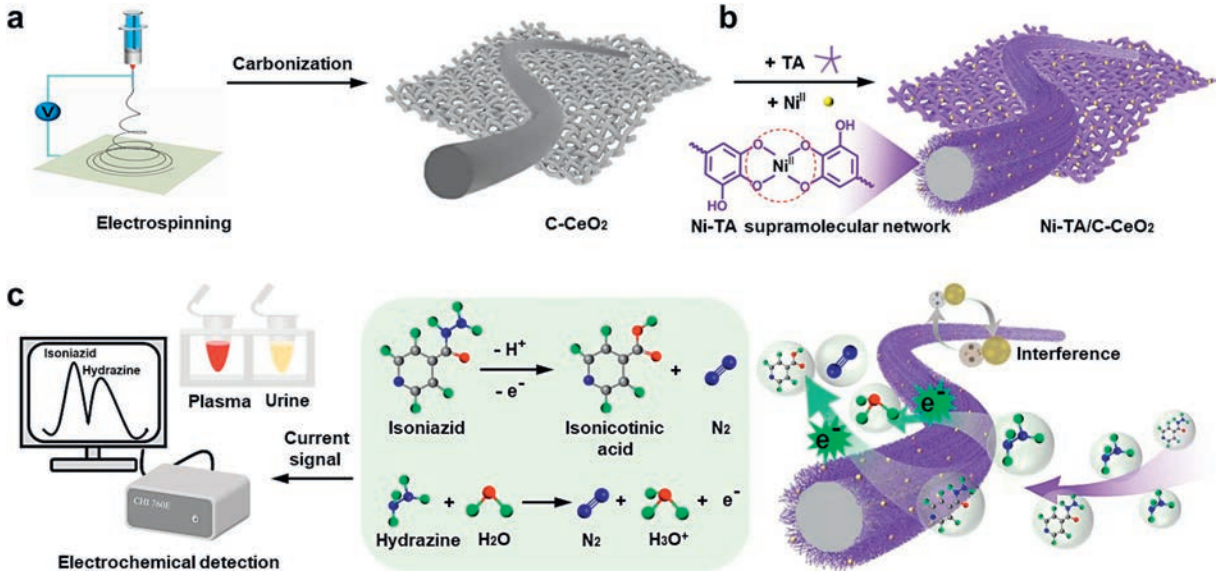

Scheme 1. Schematic representations of (a) the preparation of C–CeO_2 nanofiber, (b) the preparation of Ni–TA network on C–CeO_2 nanofiber, and (c) the possible mechanism of Ni–TA/C–CeO_2 for INZ and HYD electrochemical detection.

nolic building blocks and metal ions through metal coordination [12,13]. Our group and others have recently been exploring these promising materials for energy and environmental applications [14,15]. Particularly, the native properties of polyphenols enable MPNs deposition onto various substrate materials, allowing for the rational design of functional films [16,17]. Additionally, the functionality of MPNs can be tuned through careful choice of the incorporated metal ions [18–20]. Caruso *et al.* demonstrated that MPNs constructed from Ni^{II} are able to distribute in a way to specifically form strong interactions with the histidine and/or methionine residues of the Fc region of antibodies for enhanced targeting [21]. Therefore, we anticipate that constructing Ni^{II}-incorporated MPN on C–CeO_2 nanofiber could generate an ideal interface to interact with amino-abundant INZ and HYD molecules, thus enabling highly sensitive electrochemical detection of INZ and HYD.

In this study, we have developed a high-performance nanostructured electrode material composed of electrospun-derived C–CeO_2 nanofiber and Ni–tannic acid-based surface, also referred to as Ni–TA/C–CeO_2 (Schemes 1a and b). Mechanistic investigations demonstrate that electronegative and hydrophilic Ni–TA facilitates the mass and electron transfer in the electrooxidation reactions of INZ and HYD. Accordingly, Ni–TA/C–CeO_2 achieves low detection limits and wide linearity ranges for INZ (0.012 μmol/L and 0.1–400 μmol/L, respectively) and HYD (0.008 μmol/L and 0.015–1420 μmol/L, respectively) in the physiological condition, outperforming native C–CeO_2 nanofiber and previously reported materials [22–24]. The performance of our materials for the simultaneous detection of INZ and HYD in human plasma and urine samples suggests great promise in real-world clinical applications (Scheme 1c).

The scanning electron microscopy (SEM) image of Fig. 1a reveals that C–CeO_2 is composed of nanofibers with a mean diameter of 65 nm. The transmission electron microscopy (TEM) image of Fig. 1b further confirms that C–CeO_2 has a relatively smooth surface. As shown in Schemes 1a and b, the construction of the Ni–TA layer on C–CeO_2 is a two-step process, including the TA adsorption on the C–CeO_2 surface and the coordination reaction between the adsorbed TA and the newly added Ni^{II} (see the structure of TA in Fig. S1 in Supporting information) [13,25]. Because of the strong chelation ability, TA acts as a polydentate ligand and forms the four-coordinate Ni^{II} complex under alkaline conditions [13,26]. Ni^{II} acts as the "joint" and links different TA molecules, thus forming a stable Ni–TA interface on C–CeO_2. As a result, the obtained Ni–TA/C–CeO_2 has a rougher surface than C–CeO_2 and a mean diameter of 70 nm (Fig. 1c). As shown in Fig. 1d, its rough surface can be seen in the TEM image. Furthermore, the thickness of Ni–TA is calculated by the nanofiber diameters before and after surface modification with the result of 5 nm. Fig. S2 (Supporting information) shows the scanning TEM (STEM) and energy-dispersive X-ray (EDX) elemental mapping images, suggesting that the C, O, Ce, and Ni elements are uniformly distributed on Ni–TA/C–CeO_2. The EDX spectrum of Ni–TA/C–CeO_2 reveals the surface exists of C, O, Ni, and Ce with the atomic ratio of 81.15:18.69:0.10:0.07 (Fig. S3 in Supporting information).

The Fourier transform infrared (FTIR) spectra of C–CeO_2, Ni–TA/C–CeO_2, and TA are shown in Fig. 1e, confirming the successful formation of Ni–TA on C–CeO_2. Compared with C–CeO_2, Ni–TA/C–CeO_2 has a new peak at 1716 cm^{-1}, which is assigned to the C=O vibration of TA. Meanwhile, the C–O vibrational shift from 1206 cm^{-1} to 1193 cm^{-1} arises *via* the electron back-donation from Ni d-orbitals to C–O [27]. The bands in the 3402–3416 cm^{-1} region are ascribed to –OH stretching of H_2O and phenol groups. The X-ray diffraction (XRD) spectra of C–CeO_2 and Ni–TA/C–CeO_2 are shown in Fig. S4 (Supporting information), with the diffraction peaks at 26.2°, 33.0°, 47.9°, 56.1°, 58.6°, 69.7°, and 76.2°. These diffraction peaks are indexed to the (111), (200), (220), (311), (222), (400), and (331) planes of CeO_2, respectively [28]. Fig. 1f displays the C 1s X-ray photoelectron spectroscopy (XPS) spectra of C–CeO_2 and Ni–TA/C–CeO_2. In contrast to C–CeO_2, Ni–TA/C–CeO_2 has more surface C–O and C=O, and a new peak O–C=O appears, further demonstrating the successful formation of Ni–TA [29]. Meanwhile, the O 1s XPS spectra (Fig. 1g) also demonstrate that Ni–TA/C–CeO_2 has more oxygen-containing functional groups, especially the hydroxyl group. The Ce 3d XPS spectrum of Ni–TA/C–CeO_2 (Fig. S5 in Supporting information) shows the $3d_{5/2}$ and $3d_{3/2}$ spin-orbit splitting, with the components (885.9 and 908.1 eV) corresponding to Ce^{III} species and the components (883.7, 888.8, 900.6, 904.8, and 912.1 eV) corresponding to Ce^{IV} species [30]. Moreover, the Ni 2p XPS spectrum of Ni–TA/C–CeO_2 (Fig. S6 in Supporting information) shows the $2p_{3/2}$ and $2p_{1/2}$ splitting, with the components (856.7 and 875.1 eV) corresponding to Ni^{II} species [31].

The surface properties of Ni–TA/C–CeO_2 were studied by time-settlement behavior, zeta potential analysis and water contact an-

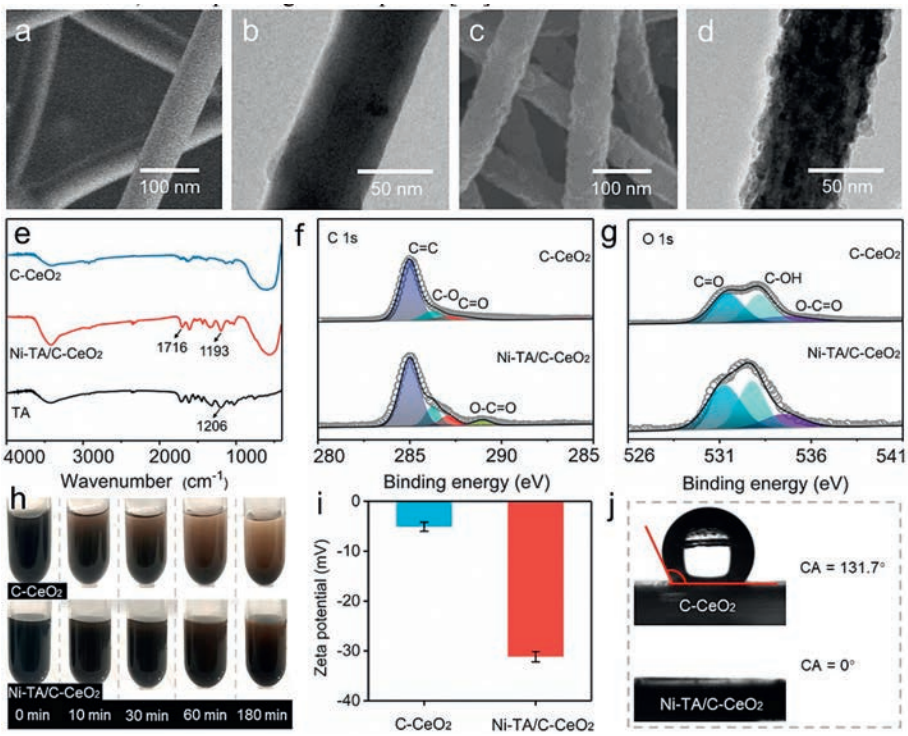

Fig. 1. Physicochemical Characterization. (a) SEM, and (b) TEM images of C–CeO_2. (c) SEM and (d) TEM images of Ni–TA/C–CeO_2. (e) FTIR spectra of C–CeO_2, Ni–TA/C–CeO_2, and TA. XPS spectra in the (f) C 1s and (g) O 1s regions for C–CeO_2 and Ni–TA/C–CeO_2. (h) Images displaying the dispersion stability of C–CeO_2 and Ni–TA/C–CeO_2. (i) zeta potential of C–CeO_2 and Ni–TA/C–CeO_2. (j) Contact angles of water on the surfaces of C–CeO_2 and Ni–TA/C–CeO_2.

gle measurement. As shown in Fig. 1h, the time-settlement experiment demonstrates that the dispersion stability of Ni–TA/C–CeO_2 is much higher than C–CeO_2. In water, most of C–CeO_2 is precipitated in 10–30 min. However, the Ni–TA/C–CeO_2 suspension shows a good dispersion even after 180 min, which can be ascribed to the decoration of electronegative Ni–TA [32]. Therefore, its surface charge property was further investigated by using the zeta potential analysis. As shown in Fig. 1i, the zeta potential value of C–CeO_2 is -5.07 ± 0.90 mV in water. The Ni–TA functional layer decreases the zeta potential of Ni–TA/C–CeO_2 to -31.13 ± 1.03 mV. Meanwhile, the zeta potential of Ni–TA/C–CeO_2 decreases with the increment of the Ni^{II}/TA ratio (Fig. S7 in Supporting information), suggesting the quantitative introduction of Ni^{II} sites. These results suggest that the Ni–TA layer enhances the electronegativity of the C–CeO_2 surface, which significantly improves the dispersion stability of the Ni–TA/C–CeO_2 suspension. The wettability of electrode material significantly influences its mass transport and thus affects the detection performance [33]. Therefore, water contact angle measurement was then conducted to analyze the surface wetting properties of C–CeO_2 and Ni–TA/C–CeO_2. As shown in Fig. 1j, the water contact angle of C–CeO_2 is as high as 131.7°. However, the water droplet can completely spread over the surface of Ni–TA/C–CeO_2. It confirms that Ni–TA/C–CeO_2 is highly hydrophilic, allowing efficient transport of analytes from the aqueous electrolyte to the electrode surface.

The adsorption properties of Ni–TA/C–CeO_2 towards INZ and HYD were investigated by batch experiments and kinetics studies. Time-dependent adsorption capacities (Q_t) are shown in Figs. 2a and b, demonstrating that Ni–TA could accelerate mass transport in the heterogeneous reaction. Figs. 2c and d show that the adsorption capacities at equilibrium (Q_e) increase with the initial concentrations (C_0), where Q_e is obtained by Eq. S1 (Supporting information) [34]. It can be attributed to the collision between adsorption sites and solutes in the high-concentration solution. The maximum Q_e of C–CeO_2 towards INZ and HYD are 5.06 mg/g and 7.03 mg/g, respectively. The maximum Q_e of Ni–TA/C–CeO_2 towards INZ and HYD are 16.93 mg/g and 18.22 mg/g, respectively. Figs. S8 and S9 (Supporting information) show the fitted adsorption isotherms for Langmuir and Freundlich models, respectively. The related values are obtained by Eqs. S2 and S3 (Supporting information) [34]. From the model constants in Table S1 (Supporting information), both INZ and HYD adsorption processes follow the Langmuir model which is usually applied to describe monolayer adsorption. The calculated maximum adsorption capacity (Q_m) of C–CeO_2 towards INZ and HYD are 5.32 mg/g and 6.94 mg/g, respectively. The calculated Q_m of Ni–TA/C–CeO_2 towards INZ and HYD are 16.67 mg/g and 20.16 mg/g, respectively. Figs. S10 and S11 (Supporting information) display the fitted kinetic models for *pseudo*-first-order and *pseudo*-second-order kinetics, respectively. From the correlation coefficients (R^2), both INZ and HYD adsorption obey *pseudo*-second-order kinetics. The related values of Table S2 (Supporting information) are obtained by Eqs. S4 and S5 (Supporting information), where the calculated Q_e and rate constant (k) are obtained from the intercept and slope by plotting t against $\ln(Q_e-Q_t)$ [35]. The k of C–CeO_2 towards INZ and HYD are 0.075 g mg^{-1} h^{-1} and 0.047 g mg^{-1} h^{-1}, respectively. The k of Ni–TA/C–CeO_2 towards INZ and HYD are 0.091 g mg^{-1} h^{-1} and 0.062 g mg^{-1} h^{-1}, respectively. The enhanced k demonstrates Ni–TA is beneficial for mass transport in INZ and HYD detection.

Cyclic voltammetry (CV) and alternating-current (AC) impedance measurements were carried out to evaluate the electrochemical performance of Ni–TA/C–CeO_2. As shown in Fig. 2e, the anodic peak current (I_{pa}) from Ni–TA/C–CeO_2 is much higher than that of C–CeO_2 and bare carbon paper (CP), suggesting faster charge transfer efficiency of the Ni–TA/C–CeO_2. As shown in the Nyquist plots (Fig. 2f), the charge transfer resistances of bare CP, C–CeO_2, and Ni–TA/C–CeO_2 are 705, 417, and 56 Ω, respectively. The impedance of Ni–TA/C–CeO_2 in the high-frequency range is

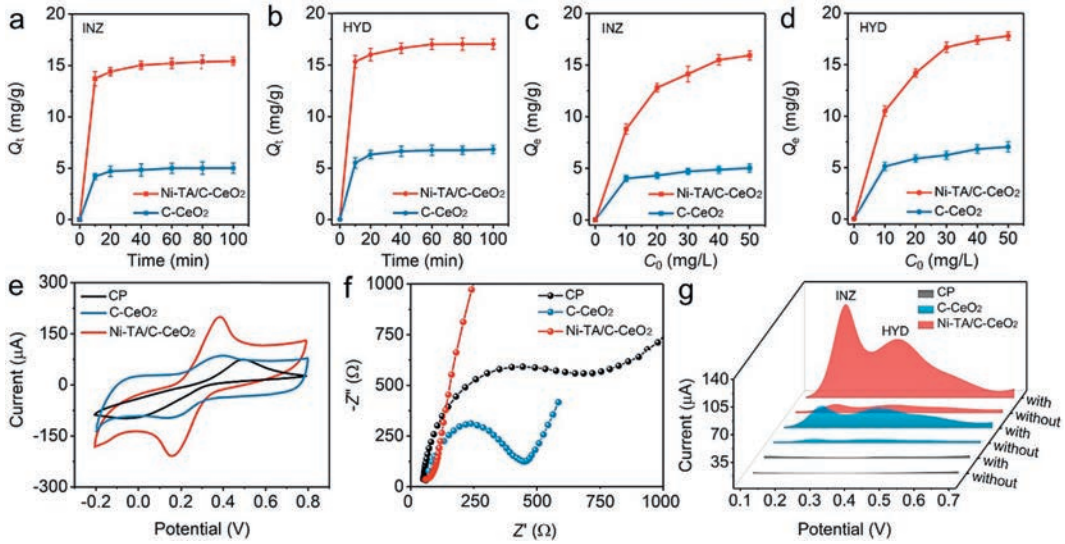

Fig. 2. Adsorption property and electrochemical performance. Relationship between Q_t and time: (a) INZ, (b) HYD. Relationship between Q_e and C_0: (c) INZ, (d) HYD. (e) CV curves, and (f) Nyquist plots of CP, C–CeO_2 and Ni–TA/C–CeO_2 in the potassium ferricyanide solution. (g) DPV curves of CP, C–CeO_2 and Ni–TA/C–CeO_2 in the 0.1 mol/L PBS solution (pH 7.0) containing 90 μmol/L INZ and 60 μmol/L HYD.

much lower than that of CP and C–CeO_2, revealing that the charge transfer of Ni–TA/C–CeO_2 is easier than that of CP and C–CeO_2. To evaluate the electrochemical active surface area (EASA), CV measurements of C–CeO_2 and Ni–TA/C–CeO_2 were performed using various scan rates (Figs. S12a and b in Supporting information). As shown in Figs. S12c and d (Supporting information), the relationship between I_{pa} and the square root of scan rate ($v^{1/2}$) is linear. According to the Randles-Sevcik Eq. S6 (Supporting information) [36], the EASA of Ni–TA/C–CeO_2 is calculated to be 0.29 cm^2, which is larger than that of C–CeO_2 (0.12 cm^2). According to the Laviron Eq. S7 (Supporting information) [37], the charge-transfer rate (k_s) of Ni–TA/C–CeO_2 is calculated to be 0.22 s^{-1}, which is higher than that of C–CeO_2 (0.14 s^{-1}). The calculated results demonstrate that Ni–TA functional layer could accelerate the mass and electron transfer between the solution and C–CeO_2 nanofiber. As shown in Fig. 2g, the current responses of analytes obtained on Ni–TA/C–CeO_2 are much higher than that of CP and C–CeO_2. These results reveal that Ni–TA functional layer could accelerate the mass and electron transfer of C–CeO_2 nanofiber, and thus enhance the current responses of INZ and HYD. To optimize the detection performance, pH conditions and Ni/TA ratio were investigated by comparative experiments. As shown in Fig. S13 (Supporting information), Ni–TA/C–CeO_2 exhibits the maximum response for the analytes in pH 7.0 electrolyte. Moreover, the peak potentials (E_{pa}) for both analytes have negative linear relationships with the pH of the electrolyte, satisfying the equation $E_{pa} = -0.056\,pH + 0.595$ ($R^2 = 0.980$) for INZ and $E_{pa} = -0.054\,pH + 0.728$ ($R^2 = 0.998$) for HYD. The slope values are 0.056 V/pH and 0.054 V/pH, respectively. They both are close to the Nernst theoretical value (0.059 V/pH), indicating equal numbers of proton and electron transfer are involved in the electrooxidation reactions [38]. The possible electrooxidation mechanisms of INZ and HYD can be expressed as Eqs. S8 and S9 (Supporting information), respectively [2,39]. As shown in Fig. S14 (Supporting information), Ni–TA/C–CeO_2 exhibits the maximum response when the ratio of Ni to TA is 0.35.

Differential pulse voltammetry (DPV) which is more sensitive to the trace detection of organic compounds was carried out to evaluate the detection performance of Ni–TA/C–CeO_2. As shown in Fig. 3a, the peak current gradually increases with INZ concentration increasing from 0 to 400 μmol/L (Fig. S15 in Supporting information). As shown in Fig. 3b, the corresponding calibration curve of INZ satisfies the equation of $I_{INZ} = 1.17C_{INZ} + 13.00$ ($R^2 = 0.991$). As shown in Fig. 3c, the peak current gradually increases with HYD concentration increasing from 0 μmol/L up to 1420 μmol/L (Fig. S16 in Supporting information). As shown in Fig. 3d, the corresponding calibration curves of HYD satisfy the equation of $I_{HYD} = 1.18C_{HYD} + 10.68$ ($R^2 = 0.995$) in the concentration range from 0.015 μmol/L to 70 μmol/L and the equation of $I_{HYD} = 0.38C_{HYD} + 69.71$ ($R^2 = 0.994$) in the concentration range from 150 μmol/L to 1420 μmol/L. The slope in the first concentration section is higher than that in the second concentration section, demonstrating a higher sensitivity in the first concentration section. This is because the electrooxidation reaction is a diffusion-controlled process, which can be demonstrated by the following kinetics study. The kinetics of INZ and HYD electrooxidation on the surface of Ni–TA/C–CeO_2 was investigated by using CV measurements with various scan rates. As shown in Fig. S17 (Supporting information), the oxidation peak current of INZ and HYD is linearly increased with the square root of the scan rate, satisfying the regression equation of $I_{INZ} = 16.57v^{1/2} - 21.16$ ($R^2 = 0.995$) and $I_{HYD} = 32.67v^{1/2} - 36.45$ ($R^2 = 0.997$), respectively. Moreover, the increase in the scan rate causes a positive shift in the oxidation peak potential. These demonstrate that the electrooxidation reaction of INZ and HYD is a diffusion-controlled process.

Furthermore, the detection limits of INZ and HYD are calculated to be 0.012 μmol/L and 0.008 μmol/L (S/N = 3), respectively. The comparison of the detection performance with other electrodes is summarized in Tables S3 and S4 (Supporting information). It should be stressed that Ni–TA/C–CeO_2 compares favorably with previously reported electrodes. Simultaneous detection of INZ and HYD was also carried out by DPV. Fig. 3e shows two well-separated peaks, which are ascribed to INZ and HYD respectively. The peak currents gradually increase with the INZ and HYD concentrations increasing. Fig. 3f shows the regression equation of INZ, determined to be $I_{INZ} = 1.15C_{INZ} - 4.57$ ($R^2 = 0.998$) in the concentration range from 0 to 265 μmol/L. Besides, the regression equations of HYD are determined to be $I_{HYD} = 0.96C_{HYD} - 5.14$ ($R^2 = 0.992$) in the concentration range from 0 to 90 μmol/L and to be $I_{HYD} = 0.36C_{HYD} + 58.16$ ($R^2 = 0.999$) in the concentration range from 140 μmol/L to 450 μmol/L. These results verify the feasibility of simultaneous detection of INZ and HYD using Ni–TA/C–CeO_2.

With high response and low background, 0.20 V and 0.40 V are demonstrated as the optimal working potentials for the amperometric tests of INZ and HYD, respectively (Fig. S18 in Sup-

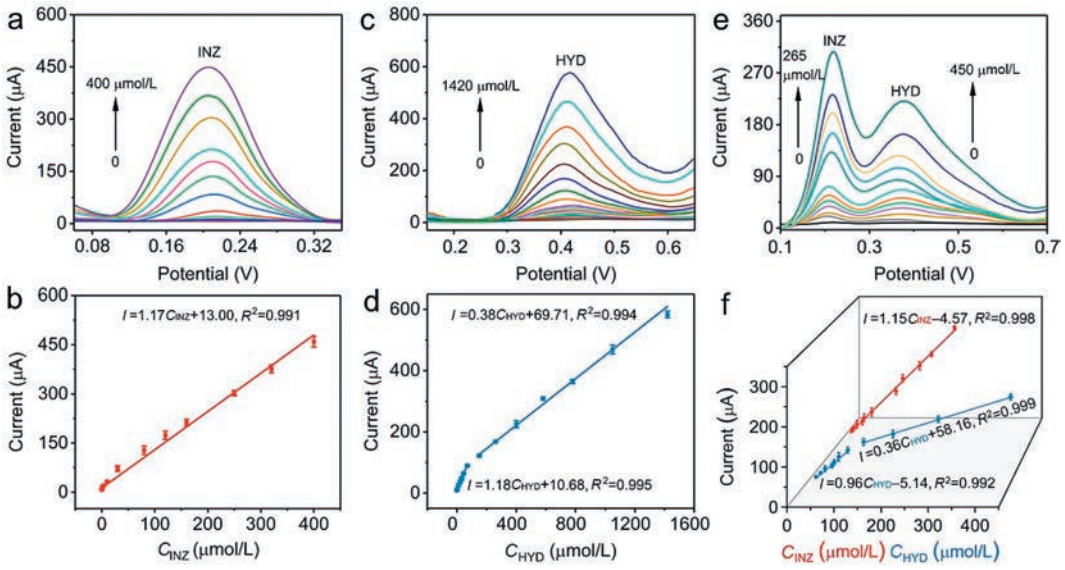

Fig. 3. Detection performance of Ni–TA/C–CeO_2. (a) DPV curves to different concentrations of INZ, and (b) corresponding calibration curve. (c) DPV curves to different concentrations of HYD, and (d) corresponding calibration curves. (e) Simultaneous detection of INZ and HYD, and (f) corresponding calibration curves.

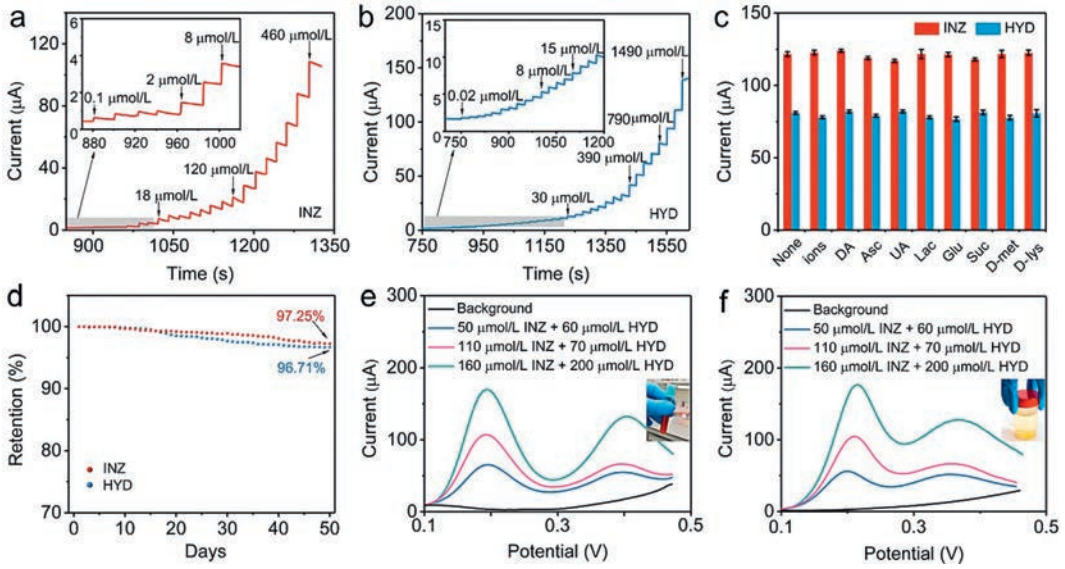

Fig. 4. Practicability of Ni–TA/C–CeO_2. Amperometric responses to the successive addition of (a) INZ and (b) HYD. (c) Amperometric responses towards INZ and HYD in the presence of interfering substances. (d) Stability tests for the simultaneous detection of INZ and HYD. DPV curves of the analyzed samples containing (e) human plasma and (f) human urine.

porting information). Accordingly, the optimal working potentials are conducted to evaluate the detection performance of Ni–TA/C–CeO_2 if not specified. As shown in Fig. 4a, the response current gradually increases during the successive addition of INZ. The response current of INZ exhibits a wide linearity range from 0.1 μmol/L to 460 μmol/L (Fig. S19 in Supporting information), satisfying the equation of $I_{INZ} = 0.20C_{INZ} + 0.86$ ($R^2 = 0.990$). Meanwhile, the response current of HYD also gradually increases during its successive addition (Fig. 4b). The response current of HYD has two linearity ranges from 0.02 μmol/L to 42.93 μmol/L and from 135.50 μmol/L to 1490 μmol/L (Fig. S20 in Supporting information), satisfying the equations of $I_{HYD} = 0.40C_{HYD} + 1.73$ ($R^2 = 0.994$) and $I_{HYD} = 0.08C_{HYD} + 13.02$ ($R^2 = 0.998$), respectively. The excellent performance of Ni–TA/C–CeO_2 could be ascribed to the accelerated mass and electron transfer.

Selectivity, stability, and repeatability are essential factors influencing practical application. The interfering substances (Na^+, Cl^-, K^+, Fe^{3+}, DA, Asc, UA, Lac, Glu, Suc, D-Met, D-Lys) with a concentration of 500 μmol/L were adopted to discuss the influence of coexisting substances on the response current of Ni–TA/C–CeO_2. As shown in Fig. 4c, the response currents from 90 μmol/L INZ and 60 μmol/L HYD are insignificantly affected by these interfering substances. In addition, the response currents are also not affected by these interfering substances in the absence of INZ and HYD (Fig. S21 in Supporting information). It demonstrates that Ni–TA/C–CeO_2 has excellent selectivity for INZ and HYD detection. The stability was then assessed by testing the concentration of INZ and HYD for 50 days on the same working electrode (Fig. 4d). During the whole process, the relative standard deviations (RSDs) are calculated to be only 1.3% and 1.9% for INZ and HYD, respectively. The repeatability was investigated by measuring the response currents of the same electrolyte on eight as-prepared electrodes (Fig. S22 in Supporting information). RSDs are only 0.73% and 0.67% for INZ and HYD, respectively. The XRD and XPS spectra before and after use also indicate that Ni–TA/C–CeO_2 has excellent stability and reproducibility (Fig. S23 in Supporting information). These results suggest that

Ni–TA/C–CeO_2 is a promising electrode material for analyzing biological samples. Therefore, the feasibility of the established electrochemical sensor in the clinical application was verified by detecting INZ and HYD in human plasma and urine samples using the standard addition method. The samples were collected from patients in the clinical laboratory with the approval of the Ethics Committee of the hospital. After adding three groups of INZ and HYD with different concentrations to the human plasma samples, the recoveries for INZ and HYD are in the ranges of 97.76%−99.20% and 98.33%−100.83%, respectively (Fig. 4e and Table S6 in Supporting information). After adding three groups of INZ and HYD with different concentrations to the human urine samples, the recoveries for INZ and HYD are in the range of 97.97%−98.23% and 97.62%−101.77%, respectively (Fig. 4f and Table S7 in Supporting information). For comparison, high-performance liquid chromatography (HPLC) methodology was also used to detect INZ and HYD in human plasma and urine samples, which agrees with the result measured by the DPV technique (Tables S6 and S7). These results suggest that Ni–TA/C–CeO_2 has high accuracy and precision in the analysis of complex plasma and urine samples in human-based samples.

Our study utilizes the polyphenol-based surface functionalization strategy to prepare Ni–TA/C–CeO_2 for the sensitive and simultaneous detection of INZ and HYD. The SEM, TEM, FTIR, XPS, EDX mapping, zeta potential analysis, contact angle measurement and time-settlement experiment are conducted to demonstrate the formation of the Ni–TA layer and analysis the surface properties. Adsorption kinetics and electrochemical characterizations reveal that Ni–TA/C–CeO_2 has strong adsorption and efficient mass transport of analyte molecules and electrons. In a physiological condition, Ni–TA/C–CeO_2 exhibited a wide linearity range for INZ (0.1–400 μmol/L) and for HYD (0.015–1420 μmol/L). Ni–TA/C–CeO_2 also exhibits low detection limits for INZ (0.012 μmol/L) and HYD (0.008 μmol/L), respectively. In the simultaneous detection of INZ and HYD, Ni–TA/C–CeO_2 has two well-separated peaks with the peak currents increasing linearly with the concentrations of INZ and HYD, verifying the feasibility of simultaneous detection. Furthermore, Ni–TA/C–CeO_2 exhibits high sensitivity, selectivity, stability, repeatability, and excellent practicability for analyzing biological samples. These results endow Ni–TA/C–CeO_2 with great potential applications in clinical diagnosis and nursing.

Declaration of competing interest

The authors declare that they have no known competing financial interests or personal relationships that could have appeared to influence the work reported in this paper.

Acknowledgments

This work was supported by Cooperative Education Program of the Ministry of Education, China (Nos. 202101256027 and 202102070134), National Excellent Young Scientists Found (No. 00308054A1045), National Key R&D Program of China (No. 2022YFA0912800), National Natural Science Foundation of China (No. 22178233), Talents Program of Sichuan Province, Double First Class University Plan of Sichuan University, State Key Laboratory of Polymer Materials Engineering (No. sklpme 2020-03-01), and Sichuan Tianfu Emei Project (No. 2022-EC02-00073-CG).

Supplementary materials

Supplementary material associated with this article can be found, in the online version, at doi:10.1016/j.cclet.2023.109113.

References

[1] P. Veerakumar, A. Sangili, S.M. Chen, et al., ACS Appl. Nano Mater. 4 (2021) 4562–4575.
[2] A. Pathak, B.D. Gupta, Sens. Actuator. B: Chem. 326 (2021) 128717.
[3] J. Han, X. Yue, J. Wang, et al., Chin. Chem. Lett. 31 (2020) 1508–1510.
[4] R.P. Jayanti, N.P. Long, N.K. Phat, et al., Pharmaceutics 14 (2022) 990.
[5] Y. Zhang, X. Jiang, J. Zhang, et al., Biosens. Bioelectron. 130 (2019) 315–321.
[6] X. Zhang, J. Zheng, Appl. Surf. Sci. 493 (2019) 1159–1166.
[7] G. Maduraiveeran, M. Sasidharan, V. Ganesan, Biosens. Bioelectron. 103 (2018) 113–129.
[8] A. Buffa, D. Mandler, Chem. Eng. J. 359 (2019) 130–137.
[9] W. Song, J. Ji, K. Guo, et al., Chin. Chem. Lett. 33 (2022) 935–938.
[10] Z. Zhu, H. Tao, J. Fu, et al., Chin. Chem. Lett. 34 (2023) 107476.
[11] K. He, T.T. Tsega, X. Liu, et al., Angew. Chem. Int. Ed. 58 (2019) 11903–11909.
[12] H. Ejima, J.J. Richardson, K. Liang, et al., Science 341 (2013) 154–157.
[13] J. Guo, Y. Ping, H. Ejima, et al., Angew. Chem. Int. Ed. 53 (2014) 5546–5551.
[14] W. Luo, G. Xiao, F. Tian, et al., Energy Environ. Sci. 12 (2019) 607–614.
[15] Y. Wang, Y. He, Q. Wang, et al., Matter 6 (2023) 260–273.
[16] J. Pan, G. Gong, Q. Wang, et al., Nat. Commun. 13 (2022) 2117.
[17] Y. Ju, H. Liao, J.J. Richardson, et al., Chem. Soc. Rev. 51 (2022) 4287–4336.
[18] K. Li, G. Xiao, J.J. Richardson, et al., Adv. Sci. 6 (2019) 1801688.
[19] Y. Xie, S. Chen, X. Peng, et al., Bioact. Mater. 16 (2022) 95–106.
[20] X. Wang, T. Hu, B. Hu, et al., J. Hazard. Mater. 431 (2022) 128441.
[21] W. Zhang, Q.A. Besford, A.J. Christofferson, et al., Nano Lett 20 (2020) 2660–2666.
[22] B.G. Santos, J.M. Goncalves, D.P. Rocha, et al., Sens. Actuator. B: Chem. 4 (2022) 100073.
[23] J. Wang, J. Zhao, J. Yang, et al., Microchim. Acta 187 (2020) 1–8.
[24] J. Yang, L. Yang, X. Tang, et al., Sens. Actuator. B: Chem. 351 (2022) 130967.
[25] J. Feng, G. Lang, T. Li, et al., J. Environ. Manage. 319 (2022) 115619.
[26] J. Guo, B.L. Tardy, A.J. Christofferson, et al., Nat. Nanotechnol. 11 (2016) 1105–1111.
[27] Y. Guo, Q. Sun, F.G. Dai, X. Chen, Adv. Mater. 33 (2021) 2007356.
[28] C. Mardani, M.Y. Rizal, R. Saleh, A. Taufik, S. Yin, Appl. Surf. Sci. 530 (2020) 147297.
[29] D. Li, C. Liu, Y. Liu, et al., Appl. Surf. Sci. 591 (2022) 153172.
[30] S. Zhao, Y. Xue, Z. Wang, et al., Mater. Chem. Front. 5 (2021) 4153–4159.
[31] M. Wang, L. Yang, B. Hu, et al., Biosens. Bioelectron. 113 (2018) 16–24.
[32] J.H. Kim, J.Y. Oh, Y.E. Shin, et al., Carbon 144 (2019) 402–409.
[33] H. Sun, Z. Yan, F. Liu, et al., Adv. Mater. 32 (2020) 1806326.
[34] Y. Mei, Y. Qi, J. Li, et al., J. Taiwan Inst. Chem. E 113 (2020) 363–371.
[35] T. Yao, W. Jia, X. Tong, et al., J. Colloid Interface. Sci. 527 (2018) 214–221.
[36] Y. Song, X. Li, C. He, Chin. Chem. Lett. 32 (2021) 1106–1110.
[37] E. Laviron, J. Electroanal. Chem. 52 (1974) 395–402.
[38] V. Main, B. Dinesh, S.M. Chen, R. Saraswathi, Biosens. Bioelectron. 53 (2014) 420–427.
[39] J. Feng, G. Lang, T. Li, et al., Appl. Surf. Sci. 604 (2022) 154548.